Journal of CO2 Utilization 83 (2024) 102810

Contents lists available at ScienceDirect

Journal of CO2 Utilization

journal homepage: www.elsevier.com/locate/jcou

Influence of morphology and composition of spherical layered double hydroxide particles and derived mixed oxides on photocatalytic CO_2 reduction

Manuel Molina-Muriel [a,b], Mahesh Eledath-Changarath [c], Archit Dhingra [c], Josep Albero [a], Juan Francisco Sánchez-Royo [c], Antonio Ribera [b,*], Hermenegildo García [a]

[a] Instituto de Tecnología Química CSIC-UPV, Universitat Politècnica de València and Consejo Superior de Investigaciones Científicas, Universitat Politècnica de València, Av. de los Naranjos s/n, Valencia 46022, Spain
[b] Departamento de Química Inorgánica, Universitat de València, Carrer del Doctor Moliner, 50, Burjassot, Valencia 46100, Spain
[c] Institut de Ciència dels Materials de la Universitat de València (ICMUV), Universitat de València, Carrer del Catedrátic José Beltrán Martinez, 2, Paterna, Valencia 46980, Spain

ARTICLE INFO

Keywords:
Solar energy conversion
Photocatalysis
CO_2 photoreduction
Ti-based layered double hydroxides
Mixed metal oxides
Methane selectivity

ABSTRACT

Considering the flexibility in the synthesis that allows the formation of materials with more than two metals, the present study reports the preparation of trimetallic layered double hydroxides (LDHs) having Al as structural tri-positive cation, Ti as photocatalytically active d^0 transition metal and either Ni or Co as dipositive cation. In addition, these LDHs were used as precursors of the corresponding trimetallic mixed oxides (MO). LDH and MO materials in combination with $Ru(bpy)_3Cl_2$ as photosensitizer and triethanolamine as sacrificial electron donor were used as catalysts for CO_2 reduction under solar light irradiation. A different product selectivity, either CH_4 for Ni-LDH or CO and H_2 for Co-MO, was observed with production rates for CH_4 or CO that are among the highest reported for these systems. The role of the inorganic materials in the photocatalytic process was supported by transient absorption spectroscopy that revealed the quenching of the $Ru(bpy)_3Cl_2$ triplet excited state by Ni-LDH or Co-MO. An important finding was that the trimetallic Co-Ti-Al oxide with cobaltite structure is able to perform CO_2 reduction in spite that the reduction potential of its conduction band is not sufficient to perform the process, evidence by photoluminescence revealing the existence of an upper electronic state responsible for the reduction. These results show the interest in screening multimetallic materials in photocatalysis due to their improved performance and diverse properties.

1. Introduction

Finding new forms of clean energy that do not emit greenhouse gases has been recently one of the main focusses of the scientific community [1,2]. In such trend, clean ways to capture and transform the CO_2 into fuels or chemicals using solar light or renewable electricity plays an important role [3–5]. CO_2 conversion often requires a catalyst that lowers the energy barrier of the reaction [6,7].

Photocatalysis is one of the possible paths to transform CO_2 into valuable products [8–10]. A wide variety of photocatalysts have been reported in the literature to perform CO_2 reduction, including MOFs [11,12], metal oxides [13,14], MXenes [15], carbonaceous materials [16] or heterostructures [17]. Among them, layered double hydroxides (LDH) stand as a very promising family of materials for photocatalytic applications [18–20], given their wide range of chemical composition, highly tunable structural and electronic properties, and their low preparation cost, which facilitates the scaling up of the production process if necessary [21,22].

LDHs have a brucite crystalline structure constituted by oxygen octahedra sharing the faces and having a di- or trivalent cation at the center. Depending on the proportion of tri-positive cations, the brucite sheet develops a positive charge that requires the presence of charge balancing anions occupying the inter-gallery spaces. Normally, up to one third of the octahedra cations can be exchanged by trivalent cations, since beyond this point, the high coulombic charge makes unstable the material and phase segregation starts to happen [23]. While initially

* Corresponding author.
E-mail address: antonio.ribera@uv.es (A. Ribera).

https://doi.org/10.1016/j.jcou.2024.102810
Received 9 February 2024; Received in revised form 22 April 2024; Accepted 17 May 2024
Available online 28 May 2024

LDHs were prepared with two different metal cations, such as Mg and Al, it has been shown that is possible to prepare LDHs with more than two metal ions, thus, expanding considerably the chemical composition of the resulting LDH materials. Introduction of a third metal has been revealed as a general strategy to tune and control the band gap and the position of the valence and conduction band potentials in these materials [24,25], which is one of the reasons why LDHs have been gaining increasing interest in the area of photocatalysis.

There are in the literature a large number of reports showing the photocatalytic activity of LDH [26–29]. In addition of the intrinsic photocatalytic properties of LDH, they can be easily converted into their corresponding mixed metal oxides by calcination at moderate temperatures about 400 ºC. Those mixed oxides also exhibit interesting photocatalytic properties [30–32]. Therefore, besides the direct use of LDHs as photocatalysts, they also offer the possibility to act as precursors of mixed oxide structures with two or more metal cations [33,34].

To further enhance the photocatalytic activity of LDHs and the mixed oxides derived from them, particularly to extend their photoresponse into the visible region, the use of metal complexes and organic dyes has been reported [35–38]. In these systems, the photosensitizer absorbs light and promotes electron or energy transfer to the LDH that becomes active in the wavelength range corresponding to the absorption of the dye. $Ru(bpy)_3^{2+}$, as well as Eosin Y, have been widely used as photosensitizers in combination with LDH materials [39].

However, selectivity control and H_2 evolution competition still remain bottlenecks to be overcome regarding photocatalytic CO_2 reduction [40,41]. In addition, the use of $Ru(bpy)_3^{2+}$ as photosensitizer often yields CO and H_2 as main products, CH_4 being only obtained when applying wavelength restrictions that reduce the number of incident photons, and thus decreasing the product generation rate [37,38].

In this context, the present article reports the photocatalytic activity of trimetallic NiTiAl and CoTiAl LDHs and the corresponding mixed oxides under $Ru(bpy)_3^{2+}$ photosensitization for the photocatalytic CO_2 reduction. It will be shown that the performance of the materials prepared in the present study are among the highest in the current state of the art giving methane in a selectivity over 85% with a production rate of 4.6 μmol/h that compares favorably with previously reported results. It will be shown that chemical composition, particle morphology and adequate band alignment are the main reasons behind this remarkable activity.

2. Materials and methods

2.1. Materials

$Ni(NO_3)_2{\cdot}6\,H_2O$ and triethanolamine (TEOA) were purchased from Alfa-Aesar. $Co(NO_3)_2{\cdot}6\,H_2O$, Ti(IV) bis(ammonium lactate)dihydroxide 50 wt% aqueous solution, $Al(NO_3)_3{\cdot}9\,H_2O$, $Ru(bpy)_3Cl_2{\cdot}6\,H_2O$, Ti(IV) oxide anatase powder and 10 wt% perfluorinated Nafion® resin solution were obtained from Sigma-Aldrich. Urea (99%) was purchased from Honeywell. Commercial Co_3O_4 oxide was obtained from ABCR. Anhydrous Na_2SO_4 was purchased from Scharlab. Water used in all experimental work was milliQ purity grade.

2.2. Catalyst preparation

LDH materials with different composition (CoTiAl, NiTiAl) and metal atomic ratios (2:0.5:0.5, 4:0.5:0.5) were prepared by solvothermal method already described by our group [42]. For example, for the preparation of LDH with 2:0.5:0.5 metal Co/Ni:Ti:Al ratio 0.30 g (1 mmol) of $Co(NO_3)_2{\cdot}6\,H_2O$ or $Ni(NO_3)_2{\cdot}6\,H_2O$, 0.09 g (0.25 mmol) of $Al(NO_3)_3{\cdot}9\,H_2O$, 120 μL (0.25 mmol) of a 50 wt% aqueous solution of Ti (IV) bis(ammonium lactate)dihydroxide and 0.24 g (4 mmol) of urea were dissolved in 40 ml of methanol. For LDH with 4:0.5:0.5 ratio quantities of Al and Ti precursors were halved. The resulting solution was stirred for 10 min and then transferred to a 100 ml Teflon lined stainless steel autoclave and heated at 120 °C for 24 h. After cooling down, the pale brown (in the case of CoTiAl) or green (for NiTiAl) precipitate was filtered and washed with methanol. Afterwards, the solid is dried in a desiccator under vacuum at room temperature. In order to improve the morphology of the materials, synthesis where precursor concentration was increased 10 or 20 times (keeping the same reaction volume) were also carried out.

Mixed oxides derived from synthetized LDH materials were also prepared by calcination of these LDH precursors at 400 °C for 6 h exposed to air atmosphere in a muffle furnace. The heating rate for the calcination was 1 °C/min.

Samples (all of which contain Ti and Al in its composition) were denoted with the code Mxyz, where M stands for the divalent cation present (Co or Ni), x for LDH (L) or mixed oxide (M), y is the divalent atomic ratio (2 or 4), and z is the precursor concentration in the synthesis (1, 10 or 20). For instance, sample NiL410 would denote a LDH material containing Ni as divalent cation, prepared with a M^{II}/M^{III} ratio of 4:1 and adding a concentration of precursors 10 times higher than the described above.

2.3. Materials characterization

Powder X-ray diffraction (XRD) spectra were obtained on a Philips X'PERT diffractometer equipped with a graphite monochromator (40 kV and 45 mA) using Cu Kα radiation (λ = 1.54178 Å) in the 2θ range of 5–90 degrees. CO_2 adsorption isotherms were collected in the low-pressure range at 0 °C using a Micromeritics ASAP 2010 equipment modified with a liquid circulation thermostatic bath. Sample required for the measurements were 300 mg approximately. Previously, the samples were activated at 100 °C under vacuum overnight to remove any adsorbed water. Surface area values were estimated using Dubinin-Astakov model. Field-emission scanning electron microscopy (FESEM) images and energy dispersive X-ray (EDX) data were collected on a Zeiss Ultra 55 apparatus equipped with an EDX detector. Lamellar cross-sections of the materials were obtained on specimens prepared with a focused ion beam (FIB), using Ga as the ion beam source, in a scanning electron microscope setup (Zeiss Auriga Compact). Elemental mappings, transmission electron microscopy (TEM) and high angle annular dark-field scanning transmission electron microscopy (HAADF-STEM) images of the lamellar cross-sections were recorded on a JEOL JEM 2100 F instrument equipped with an EDX detector. X-ray photoelectron spectroscopy data were obtained on a SPECS spectrometer equipped with a PHOIBOS 150 MCD-9 detector employing a non-monochromatic X-ray source (Al) operating at 200 W. XPS data were calibrated against adventitious carbon C1s at 284.6 eV.

Diffuse reflectance UV–vis spectroscopy measurements were carried out on a Perkin-Elmer Lambda 1050 spectrophotometer equipped with a Harrick Praying Mantis™ diffuse reflectance accessory. Liquid UV–vis spectroscopy measurements were performed on a Varian Cary 50 spectrophotometer. UV photoelectron spectroscopy (UPS) measurements were performed on a SPECS GmbH system (base pressure $1.0{\cdot}10^{-10}$ mbar) equipped with a PHOIBOS 150 2D-CMOS hemispherical analyzer. The photoelectrons were excited with the He I line (21.2 eV) of the He discharge source (SPECS UVS 300). Work function measurements required applying a negative external voltage to the sample with respect to the analysis chamber. An external voltage of -4.07 V, -4.04 V, -4.03 V and -4.47 V was applied to the samples CoL21, CoM210, NiL410 and NiM410, respectively. The work function is determined by subtracting the high binding energy cut-off from the incident photon energy. Transient absorption spectra (TAS) were collected using the fourth harmonic of a Q switched Nd:YAG laser (Quantel Brilliant, 266 nm, 15 mJ/pulse, 7 ns FWHM) coupled to a mLFP-122 Luzchem miniaturized detection equipment. The transient absorption photospectrometer includes a 300 W ceramic Xe lamp, 125 mm monochromator, Tektronix TDS-2001 C digitizer, compact photomultiplier, and power supply. The laser flash generates 5 V trigger pulses with programmable frequency

and delay. For the measurements, the cuvette was filled with a Ru(bpy)$_3$Cl$_2$ solution in acetonitrile that would contain both TEOA and a photocatalyst suspension, one of them, or none. Afterwards, the cuvette was purged with N_2 or CO_2 to study the quenching of the electron transfer in presence and absence of CO_2. Laser excitation wavelength was set at 450 nm, according to $Ru(bpy)_3^{2+}$ absorption spectra.

Steady-state fluorescence emission spectra of the solid samples were recorded on a FLS1100 photospectrometer (Edinburgh Instruments) equipped with double grating Czerny-Turner monochromators with 2×325 mm focal length in excitation and detection, and a PMT-980 detector covering the range 200–980 nm. A 400 W Xe lamp was used as the light source. A scan of the emission spectra was performed in the range 290–800 nm on intervals of 20 nm. In-situ FTIR experiments were performed on a Thermo Nicolet iS50 spectrophotometer equipped with a DTGS detector (4 cm^{-1} resolution, 32 cumulative scans). Self-supported pellets (13 mm diameter) containing 20 mg of photocatalyst were prepared and introduced in a home-made IR cell connected to a gas dosing system. First the photocatalyst was pretreated at 100 °C in Ar atmosphere for 1 h to remove adsorbed water molecules. Then, the system was cooled down to 50 °C (same temperature as the photocatalytic tests). A CO_2 stream (30 ml/min) was bubbled through distilled water (to provide humid CO_2) and directed to the IR cell to perform the dark experiments, recording IR spectra at 10 min intervals. For experiments under irradiation the same procedure was followed, but also irradiating the sample with the output light from a 300 W Xe lamp equipped with a 380 nm cut-off filter when exposing the material to humid CO_2.

Electrochemical impedance spectroscopy (EIS) and photocurrent measurements were carried out on a Gamry Interface 5000E potentiostat, using a three-electrode configuration in a single-compartment quartz cell. Pt and Ag/AgCl were used as counter and reference electrodes, respectively, and 0.1 M Na_2SO_4 as the electrolyte. Working electrodes were prepared by drop-casting of 40 μL of a suspension consisting of 10 mg of catalyst, 170 μL of ethanol and 23 μL of a commercial perfluorinated Nafion® resin solution (10 wt%) onto a FTO glass electrode, over an area of 1 cm^2 (1×1 cm). For EIS measurements the scanning frequency range was 0.01 Hz-100 kHz at 1 V vs Ag/AgCl. Photocurrent experiments were performed under open circuit potential conditions and using a 300 W Xe lamp as the light source. Measurements were recorded both under full spectrum range and in the UV-A/visible region, for which a 380 nm cut-off filter was equipped to the lamp.

2.4. Photocatalytic tests

Photocatalytic CO_2 reduction was performed on a closed quartz reactor (52 ml volume) equipped with an external heating ribbon to keep the system at 50 °C during the test. First, the required amount of catalyst was dispersed in 20 ml of a CH_3CN:H_2O:TEOA 3:1:1 in volume mix under vigorous stirring. The dispersion was sonicated for 15 min and then 6.6 mg of Ru(bpy)$_3$Cl$_2$·6 H_2O were added to the suspension. The dispersion was transferred to the photoreactor and preheated at 50 °C. Pure CO_2 was bubbled into the mixture for 10 min, filling the reactor with a final overpressure of 0.5 bar.

To evaluate the photoactivity of each catalyst, simulated solar irradiation was performed using the beam output of a Newport Oriel® Sol1A™ Class ABB 94041 A solar simulator equipped with a Xe arc lamp and a AM1.5 G filter. Gas phase samples were collected from the head space of the reactor after 1 h of reaction. Hydrogen evolution was quantified using a gas chromatograph (Agilent 490 MicroGC) equipped with a Mol Sieve 5 Å column and a TCD detector using Ar as the carrier gas. The amounts of CO and CH_4 produced were estimated using a gas chromatograph (Agilent 7890 A GC System) equipped with a Carboxen®-1010 PLOT Capillary GC Column with a TCD detector using He as the carrier gas.

Several blank experiments were carried out in the absence of Ru(bpy)$_3$Cl$_2$, TEOA, photocatalyst, CO_2 or irradiation source to prove the photocatalytic nature of the products generated. In addition, to prove the stability of the material several reaction cycles were performed consecutively, recovering the material from the solution by centrifugation at 9000 rpm between each of the cycles. The catalyst mass employed in those experiments was 10 mg to minimize the effect of the catalyst mass loss during the recovery process.

To prove that gaseous CO_2 is the origin of the generated products, isotopic ^{13}C experiments were performed under the same conditions, but purging the system with ^{13}C labelled CO_2. Gaseous samples were collected after 1 h of reaction. Generated products were analyzed on a gas chromatograph coupled with a mass spectrometer (Shimadzu GCMS-QP2010 Ultra).

Apparent quantum yield (AQY) experiments were carried out on the same setup but using a PLS-SXE300E 300 W Xe lamp equipped with band-pass filters centered at 365, 405 and 550 nm (13.3, 38.3 and 52.8 mW/cm^2, respectively). Light intensity for each wavelength was measured with a calibrated photodiode.

3. Results and discussion

3.1. Materials characterization

Two different LDHs, NiTiAl and CoTiAl, with two different M^{II}:M^{III}:M^{IV} atomic ratios and the corresponding mixed oxides derived therefrom were prepared in the present study for the purpose of evaluating their photocatalytic activity for CO_2 reduction. The synthesis of LDHs was performed in methanol using urea to continuously provide ammonia at 120 ºC. Scheme 1 illustrates the synthetic procedure. It has been reported in the literature that the use of methanol as solvent for the synthesis provides highly dispersible samples characterized by the stacking of a lesser number of LDH sheets [43]. As metal precursors, nitrate salts were used except for Ti^{IV} that was provided as bis (ammonium-lactate)dihydroxide since this complex enjoys better stability against hydrolysis than the more commonly used $TiCl_4$, minimizing a prompt formation of TiO_2, therefore allowing a better incorporation of Ti in the resulting material [24,39,44].

The selection of these elements, and particularly Ti in the composition, was based on the consideration of the well-known superior photocatalytic activity of Ti oxides and the role of Ni and Co as catalysts in CO_2 reduction [45–47]. Subsequent transformation of the NiTiAl and CoTiAl LDHs by calcination at 400 ºC rendered the corresponding mixed trimetallic oxides with a crystalline phase constituted by NiO or Co_3O_4 and amorphous phases of Ti and Al probably also containing Ni and Co. Table 1 lists the samples prepared in the present study indicating the elemental composition for each of the materials synthetized.

Besides different metal ratios, the synthesis was also performed at three different precursor concentrations since the morphology of the particles and crystallinity is affected by the experimental conditions of the synthesis. These structural parameters can play a significant role in the photocatalytic activity due to the influence of the specific surface area, but also the density of structural defects. Defects including oxygen vacancies can function as CO_2 adsorbing sites, but also as charge trapping centers favoring charge separation or recombination [48,49].

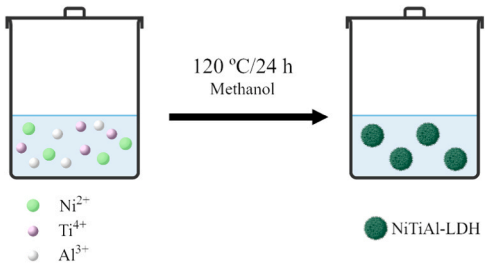

Scheme 1. Synthetic procedure of LDH materials prepared in the present study.

Table 1
Cationic ratios of the most representative materials in the present study. Surface areas estimated from CO_2 adsorption data by Dubinin-Astakhov model are also listed.

Sample	% Ni	% Co	% Ti	% Al	Surface area (m^2/g)
NiL41	70.9	/	14.4	14.7	180.1
NiL410	76.7	/	10.3	13.0	174.8
NiL420	73.0	/	8.7	18.3	206.2
NiL210	65.7	/	15.7	18.6	/
NiM410	80.9	/	7.0	12.1	691.0
CoL21	/	62.0	19.4	18.6	62.77
CoL210	/	61.3	16.7	22.0	/
CoM21	/	63.0	18.5	18.5	/
CoM210	/	59.9	16.2	23.9	230.47
CoM410	/	78.8	9.4	11.8	/

Specific surface area of the materials was measured using isothermal gas adsorption. Using N_2 to monitor area porosity resulted in very small surface area values in the range 10 m^2/g or lower. However, since the purpose of the present study is the photocatalytic conversion of CO_2, this gas was also employed for surface area measurements. Typically, the use of CO_2 results in higher specific surface area values compared to N_2 due to the smaller kinetic diameter of CO_2 (330 pm) respect to N_2 (364 pm) [50]. Thus, the use of CO_2 allows to determine the surface of ultramicropores that are not measured by N_2. In addition, the higher temperature employed for CO_2 measurements allows a better diffusion of the gas through the solid, although it disfavors adsorption. In the present case, surface areas for CO_2 measurements were above 60 m^2/g, reaching even 200 m^2/g for some samples. Table 1 also lists specific surface area for some of the best photocatalysts under study.

After the synthesis, the samples were characterized by powder X-ray diffraction, showing the expected peaks corresponding to LDH phase (JCPDS-38–0715) in the cases of all Ni and Co-based LDHs as broad signals indicating their poor crystallinity [36]. Fig. 1 shows representative XRD patterns, while supporting information Fig. S1 contains the full set of XRD data. No influence of the synthesis conditions, either the cationic ratio or precursor concentration, was observed on the position or intensity of the XRD peaks. The position of the (003) diffraction peak at 2θ value around 10° indicates that nitrate is the counter anion present in the interlayer space after the synthesis [23]. As expected, calcination of the LDH rendered the corresponding oxides. In the case of NiM410, having the highest Ni content, XRD indicates the presence only of NiO with its characteristic diffraction bands at 37.2, 43.3, 63.1, 75.6 and 79.4 degrees corresponding to the diffraction of the (111), (200), (220), (311) and (222) facets, respectively (JCPDS-78–0423) [14]. Analogously, the thermal treatment of Co-based LDHs results in the change in the XRD pattern from the initial layered material to a spinel type diffractogram, typical of Co_3O_4 (JCPDS-74–2120) [51]. Since no information about the Ti and Al phases is apparent in XRD after calcination it can be assumed that these elements should be present as amorphous

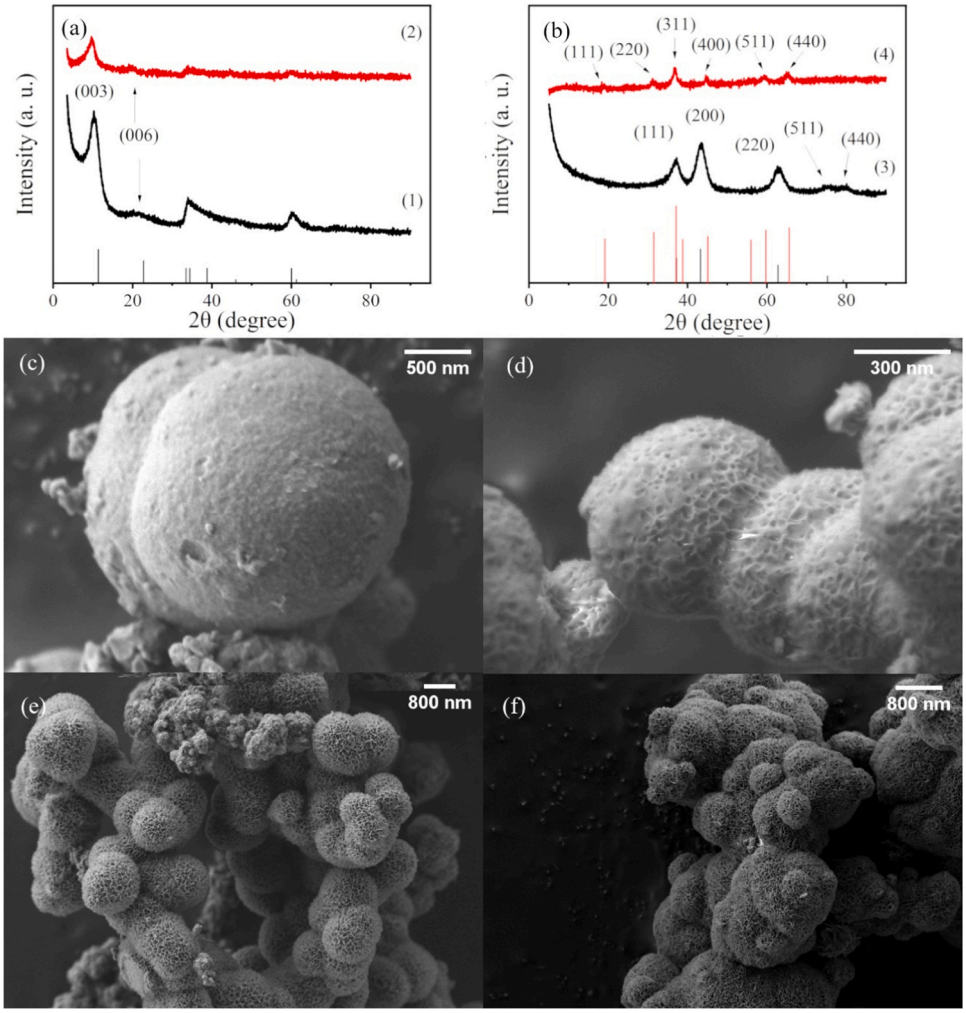

Fig. 1. XRD patterns (a-b) of NiL410 (1), CoL21 (2), NiM410 (3) and CoM210 (4). Diffraction peaks according to JCPDS database corresponding to α-$Ni(OH)_2$ (Fig. 1a), NiO (Fig. 1b, black) and Co_3O_4 cubic spinel (Fig. 1b, red) are included for reference. FESEM images of NiL410 after 2 (c), 5 (d) and 24 h (e) of synthesis. FESEM image of CoM210 (f).

oxides, probably also containing some Ni or Co.

The morphology of LDH after the synthesis was monitored by FESEM. Fig. 1 also shows selected FESEM images of some of the samples, while supporting information (Fig. S2) provides a more complete set of micrographs. As it can be seen in all these images, the most characteristic morphological feature is the presence of spheroid particles constituted by 2D sheets placed radially respect to the center. Concentration of the reagents during the synthesis influences the density of these 2D sheets that become more compact and denser as the concentration increases.

We were intrigued by this morphology and the origin of these spherical arrangements. Important information about the mechanism of particle growth was obtained by taking images at various times after mixing the reagents. In this way, it was observed that the first spherical particles appearing at short synthesis times (2 h) contained almost exclusively Ti, without having a significant percentage of the other metallic elements. It was proposed that most of the Ti-lactate complexes used as precursors during the synthesis undergo almost complete precipitation as spheres as soon as this precursor enters in contact with the reaction media. Starting from this initial stage, a second phase corresponds to the growth of the LDH using dissolved M^{II} and Al cations and mobilizing Ti^{IV} from its initial spherical particles. Thus, the growth of LDHs occurs on the surface of the spheres. Selected images to illustrate this two-step growth of NiTiAl and CoTiAl LDHs are provided in Fig. 1 as well as EDX elemental analysis showing the prevalent Ti composition of the initial nuclei appearing in the methanol phase in which almost no Al, Ni or Co are present (Table 2). The characteristic morphology and poor stacking of the 2D LDH sheets formed in methanol are responsible of the high dispersibility of these as-synthesized materials. Calcination of the LDHs preserved their spheroid shape and the 2D morphology of constituent sheets, with some shrinkage of the diameter of the spherical particles. Fig. 1 and S3 provide additional SEM images of the mixture of multimetallic oxides resulting from calcination of the pristine LDHs.

To properly understand the morphology and structure of the materials under study, TEM images of lamellar cross-sections of the spherical particles were taken (Fig. S4a). It can be seen that in some particles there is still a residual core of those initial Ti-containing nuclei, while in others, the initial Ti core has completely disappeared, and the particle is constituted by the loose agglomeration of 2D sheets. Fig. S4 also presents EDX mapping for those particles in which no core can be observed, presenting a homogeneous distribution of the three metallic elements in agreement with XRD pattern showing the formation of LDH as the only crystalline phase. HRTEM images of some representative materials (Fig. S5) also show the corresponding reflections of their crystalline phase, in accordance with XRD data. Scheme 2 illustrates our proposal to rationalize the morphology of the prepared LDH.

The elements present in the material and the surface composition was determined by survey XPS analysis and the data were in agreement with those obtained by EDX. Fig. S6 shows survey XPS data for the best performing materials of the study, while Fig. 2, S7 and S8 present high resolution XPS data for the metallic elements and O. Based on these XPS spectra, the oxidation state and coordination sphere were determined for each element. In the case of NiL410, the high resolution XPS Ni 2p has two parts due to the spin-orbit coupling, attributable to Ni $2p_{3/2}$ and Ni $2p_{1/2}$, accompanied by their corresponding satellite bands. The Ni $2p_{3/2}$ peak has a binding energy of 856.5 eV, and it has a single component attributable to Ni^{2+} [52]. The Ti spectrum has a weak intensity, but it exhibits two signals due to the spin orbit coupling, the peak of Ti $2p_{3/2}$ appearing at 460.4 eV and having a single component attributable to Ti^{4+} [53]. The weakness of XPS Ti 2p spectrum could be due to the fact that this element is not exposed to the external surface of the spherical particles, this explanation agreeing with the earlier proposal on the mechanism of particle formation. According to it, Ti would undergo an immediate precipitation forming the core of the LDH spheres and supplying from the core the Ti element for the sheet growth.

Table 2
Cationic composition of NiLDH410 at different synthesis times.

Reaction time (h)	% Ni	% Ti	% Al
2	2.3	89.9	7.8
5	79.5	6.6	13.9
24	76.7	10.3	13.0

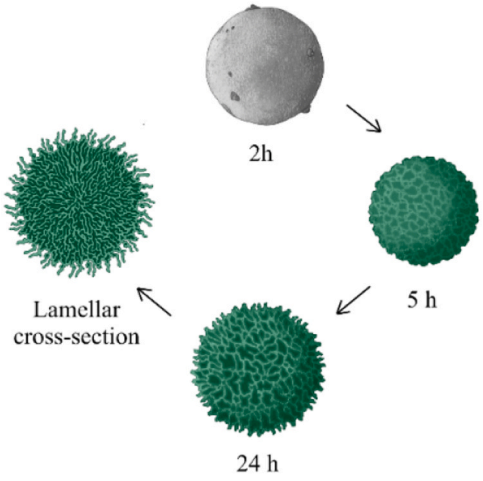

Scheme 2. Illustration of the proposed growth mechanism and particle morphology changes with synthesis time of the LDHs prepared in methanol media. At 2 h of synthesis only the core Ti particles can be observed. At 5 h, LDH sheets are still growing on the surface of the Ti particles, while at 24 h the growth process is complete. Lamellar cross-sections of the particles show that the initial Ti core is consumed during the process, and the particles are composed of a spherical aggregate of LDH sheets.

Regarding Co-containing samples, XPS analysis indicates the presence of the expected elements. For the XPS Co 2p peak, the binding energy and components of Co 2p agree with those reported in the literature for $Co(OH)_2$ (CoL21, Fig. S7) and Co_3O_4 (CoM210, Fig. 2), respectively [52]. The XPS Ti 2p peak is more intense in Co-based materials than for the Ni series and deconvolution of its spectrum indicates the presence of a component of Ti^{4+} at 458.0 eV, accompanied in the case of CoL21 with a minor (5%) component at 456.0 eV due to the presence of residual Ti^{3+} [44]. The XPS analysis of the elements in other samples prepared in the present study exhibit similar features as those commented for NiL410 and CoM210. Fig. S7 presents some examples of XPS data from these materials. XPS Al 2p data for all the materials under study present the distinct features expected for Al^{3+} spectrum, as seen in Fig. S8.

Analysis of the high-resolution O 1 s spectra of the LDH and the corresponding mixed oxide provides valuable information. In LDH materials, either containing Ni or Co, the prevalent component (over 80%) appearing around 531–532 eV corresponds to -OH, in accordance with the brucite structure. Upon calcination, and formation of the mixed oxides the peak corresponding to hydroxide disappears and then, the two relative components at 529.9 eV and 530.7 eV agree with the expected binding energy values for lattice oxygen in metal oxide and oxygen vacancies, respectively [54]. The fact that the component corresponding with oxygen vacancies is much larger in the case of NiM410 (86.8%) respect to CoM210 (69.9%) is in accordance with the significantly larger surface area of NiM410 and would indicate a larger density of defects in the former compared to the later.

Regarding photocatalytic activity, diffuse reflectance UV-Vis spectroscopy (DRS) is one of the important characterization techniques, giving information about the photoresponse of the solids. Fig. 3 presents UV–vis absorption spectra of four of the samples under study. As it can be seen there, light absorption increases upon calcination and is more intense for corresponding mixed oxides than the LDH precursors.

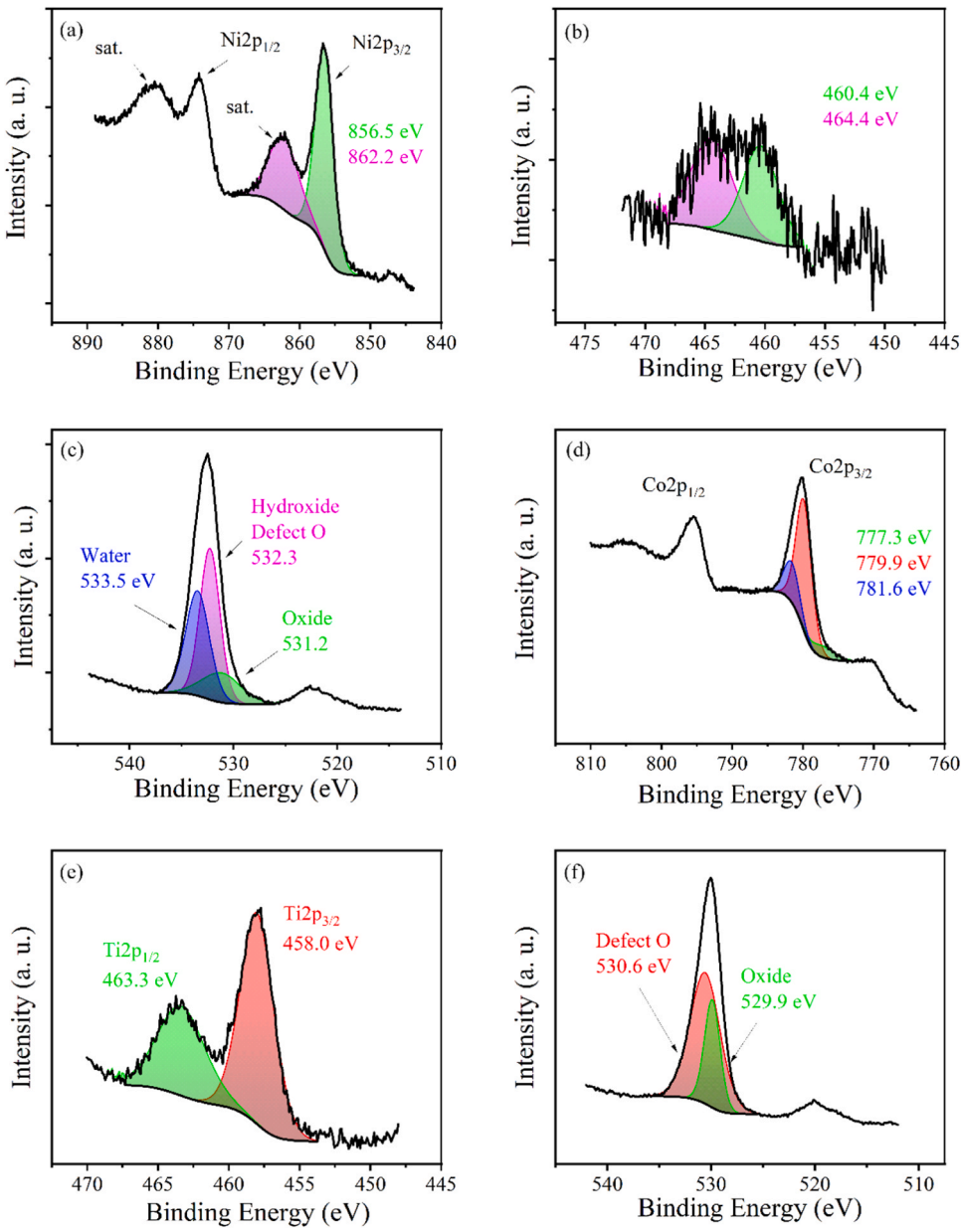

Fig. 2. High resolution XPS of NiL410: Ni 2p peak (a), Ti 2p peak (b) and O 1 s peak (c). High resolution XPS of CoM210: Co 2p peak (d), Ti 2p peak (e) and O 1 s peak (f). The plots also present the best deconvolution of each XPS peak to individual components, indicating their assignment and binding energy value.

Particularly in the case of CoM210 that is a black solid, in comparison with the green NiM410, absorption spectrum expands to the whole wavelength range from 200 to 800 nm. Recording the absorption spectrum in the NIR region (Fig. S9) shows that the absorption of CoM210 decreases abruptly at about 850 nm. The optical bandgaps of the solids were determined from Tauc plots, considering the materials as indirect semiconductors. For those samples prepared at higher precursor concentration, similar UV-Vis spectra were obtained, although with lower absorption intensity and essentially coincident bandgaps (see Fig. S9 in supporting information).

3.2. Photocatalytic experiments

Photocatalytic studies were carried out in a 52 ml quartz reactor with inlet and outlet valves. Different amounts of photocatalyst were suspended by extended sonication into a mixture of acetonitrile (12 ml), H_2O (4 ml) as proton donor and TEOA (4 ml) as electron donor. To this suspension $Ru(bpy)_3Cl_2$ was added to reach a 0.44 mM concentration. The liquid phase was then saturated with CO_2 and the system was irradiated from the top using the output of a solar simulator operating at 100 mW/cm^2. The temperature of the system was measured monitoring a value of 50 °C during the reaction. Preliminary blank controls indicate that no CO_2 reduction products appear in the gas phase in the dark, under simulated sun irradiation but absence of $Ru(bpy)_3^{2+}$ or TEOA, or if the system was filled with Ar instead of CO_2. These controls show that irradiation, CO_2, $Ru(bpy)_3^{2+}$ and TEOA are essential components to observe product evolution. The results obtained upon 1 h irradiation for a series of Ni-based LDH and mixed oxides using $Ru(bpy)_3^{2+}$ as photosensitizer and TEOA as electron donor are presented in Fig. 4. As it can be seen there, in these experiments, evolution of CH_4 was observed accompanied by minor amounts of H_2 and CO. Similar experiments using Co-based materials as photocatalysts gave a significantly different selectivity, CO being the prevalent product accompanied by similar amounts of H_2. Incidentally, the product distribution found for Co-containing materials is similar to that obtained for $Ru(bpy)_3^{2+}$ and TEOA in the absence of either LDH or mixed oxides, although the

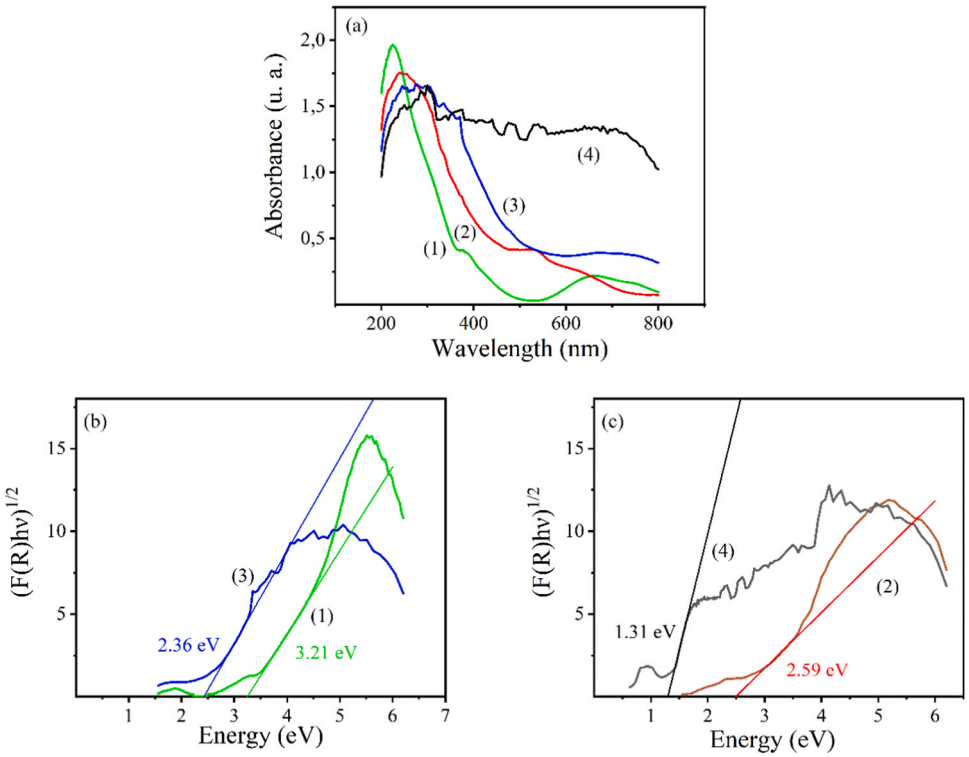

Fig. 3. UV-Vis DRS spectra (a) and Tauc plots (b-c) including estimated optical band gaps of the best performing materials under study. Sample codes are NiL410 (1), CoL21 (2), NiM410 (3) and CoM210 (4).

production rate is enhanced by a factor of three when CoM210 is present. Optimization of the amount of photocatalyst in the system shows that the optimal concentration in the case of Ni-based materials is 0.15 mg/ml, while for Co-based materials is 0.05 mg/ml, as shown in Fig. S10.

From the data shown in Fig. 4 it can be observed that in the case of Ni-based photocatalysts, the efficiency depends on a series of parameters, including the concentration of precursors in the synthesis that eventually lead to a different sheet density in the spheres, and the Ni:Ti:Al atomic ratio. In that way, the most efficient photocatalyst was NiL410 prepared at 10 times higher concentration with Ni:Ti:Al ratio of 4:0.5:0.5. Interestingly, calcination of the LDH to form the corresponding oxide derived material results in a decrease of the photocatalytic activity, although still with the same product selectivity as that of the LDH series. It should be commented that the amount of CO produced by these materials after 1 h is close to the detection limit of our instrument, which made difficult its identification in some of the experiments. It is also interesting to comment at this point that methane is not formed in a control in which $Ru(bpy)_3^{2+}$ and TEOA are used in the absence of any other material as homogeneous photocatalyst for CO_2 reduction.

As commented above, in comparison to the Ni-containing materials, one remarkable difference of the Co series is the photoproducts formed in the process. In the presence of any of the Co-based materials, CH_4 is not formed, while CO and H_2 in similar proportions are simultaneously formed. The influence of several synthesis parameters on the photocatalytic activity of the Co-containing materials was also studied as in the case of the Ni series. Different trends between Co and Ni materials were observed, as in the case of Co-LDHs, an increase in the concentration of the precursors during de synthesis, resulting in a denser packing of sheets, leads to a decrease on the photocatalytic activity. Contrary to the Ni series, calcination of the LDH results in mixed oxides with spinel structure that are more active than the corresponding LDH precursors. The Co:Ti:Al atomic ratio also exerts an influence in the photocatalytic activity, the most active material CoM210 obtained by calcination of CoL210 whose synthesis was performed using 10 times more concentrated precursors. For the calcined materials, the optimal Co:Ti:Al atomic ratio was 2:0.5:0.5.

Since Ti is an element present in all the materials under study, the photocatalytic activity of LDH and the corresponding materials derived by calcination was compared with the performance of a commercial TiO_2 sample under the same conditions. These results are also presented in Fig. 4. As it can be seen there, CO and H_2 in similar amounts are the products formed when using TiO_2. The efficiency however is about three times lower than that achieved under the same conditions with CoM210 and similar to the amounts of products obtained using only $Ru(bpy)_3^{2+}$ and TEOA without any cocatalyst. This comparison illustrates again the advantage of the use of LDHs and its derived products in this kind of photocatalytic systems.

To confirm that CO_2 is the source of CH_4 or CO obtained as photoproducts in the case of NiL410 and CoM210 respectively, isotopic ^{13}C labelled experiments were carried out. In the case of NiL410, the presence of a peak in mass spectra at m/z 17 with higher intensity than expected for fragmentation of the water was recorded. Fig. S11 in supporting information presents the mass spectrum of $^{13}CH_4$ formed upon irradiation of $^{13}CO_2$ in the presence of NiL410. Analogously, formation of ^{13}CO from $^{13}CO_2$ under photocatalytic irradiation of CoM210 was also monitored by mass spectrometry.

The stability of NiL410 and CoM210 was confirmed by performing a series of three consecutive uses of the same sample. Between each use, the catalyst was recovered by centrifugation, washed two times with fresh milliQ water and mixed with fresh solutions of $Ru(bpy)_3^{2+}$ and TEOA. The results are presented in Fig. S12. As can be seen there, a gradual decrease in the production of methane upon reuse was observed. However, this decrease in activity could be due to the loss of some photocatalytic material during the workup between two consecutive reactions. A similar trend is observed in the case of CoM210. Fig. S12 also presents SEM images of the photocatalysts recovered after three consecutive uses, showing no apparent changes in their morphology.

To put the photocatalytic activity obtained by Ni-LDH and Co-MO

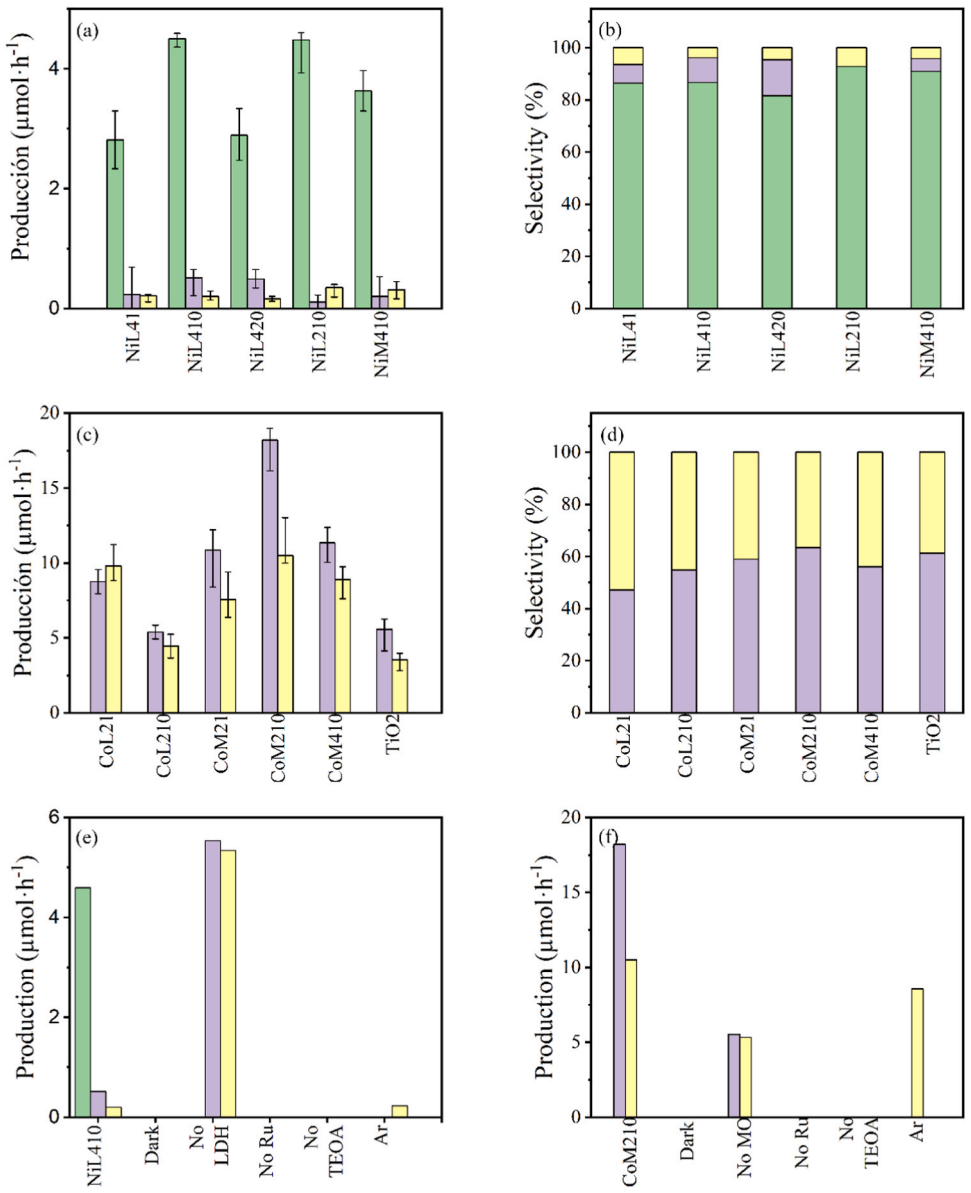

Fig. 4. Photocatalytic production (a) and selectivity (b) for photocatalytic CO_2 reduction over several Ni-based photocatalysts. Photocatalytic production (c) and selectivity (d) for photocatalytic CO_2 reduction over several Co-based photocatalysts. Control experiments for NiL410 (e) and CoM210 (f), respectively. Products generated were CH_4 (green), CO (purple) and H_2 (yellow). Reaction conditions: 20 ml of CH_3CN:H_2O:TEOA 3:1:1 solution, 3 mg (NiL410) or 1 mg (CoM210) of photocatalyst, 6.6 mg $Ru(bpy)_3Cl_2$, T: 50 ºC, solar simulator light (AM 1.5 G filter, 100 mW/cm^2).

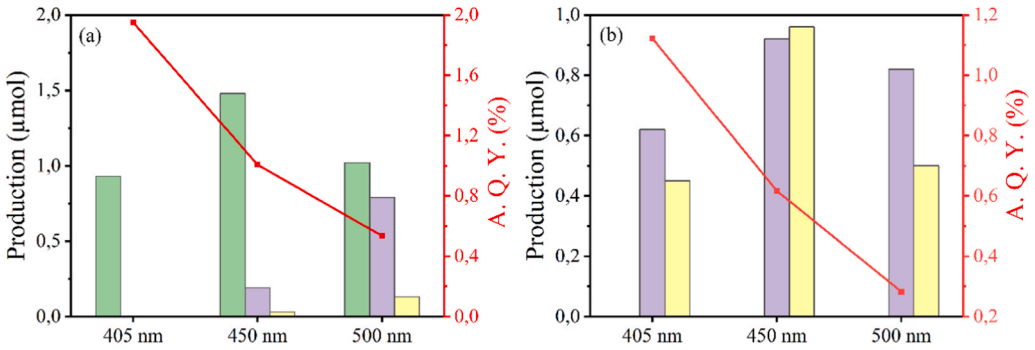

Fig. 5. Total apparent quantum yields obtained for NiL410 (a) and CoM210 (b) measured at different excitation wavelengths. Products generated were CH_4 (green), CO (purple) and H_2 (yellow). Reaction conditions: 20 ml of CH_3CN:H_2O:TEOA 3:1:1 solution, 3 mg (NiL410) or 1 mg (CoM210) of photocatalyst, 6.6 mg Ru $(bpy)_3Cl_2$, T: 50 ºC, Light source: PLS-SXE300E 300 W Xe lamp equipped with band-pass filters centered at 405, 450 and 500 nm (13.3, 38.3 and 52.8 mW/cm^2, respectively).

into a broad context, Tables S1 and S2 provide a comparison of our results with those previously reported in the literature for the same reaction. As it can be seen there, the results obtained for methane formation using NiL410 are the best reported so far. Also, it should be noted that CO rather than methane is the product commonly observed using $Ru(bpy)_3^{2+}$ as sensitizer and TEOA as electron donor [36,55]. In the case of the CoM210, for which CO is the main product, this material is ranked among the most efficient photocatalysts although its activity is far from that of hollow ZnCo-LDH [28]. However, there are many important experimental parameters that may influence the photocatalytic activity from one laboratory to another and could change the relative ranking of the photocatalysts.

To further assess the efficiency of the photocatalytic activity of NiL410 and CoM210, quantum yields of product formation were measured using monochromatic visible light. The results are presented in Fig. 5. It can be seen there that the quantum yield increases towards the UV, decreasing for longer wavelengths. Values of about 2% and 1.1% were determined for the quantum efficiency at 405 nm for NiL410 and CoM210, respectively. Considering that $Ru(bpy)_3^{2+}$ is the light harvesting component of the photocatalytic system and its absorption spectrum does not vary from one experiment to another (see Fig. S13 in supporting information), a constant quantum efficiency should be observed for the three wavelengths under study, unless the efficiency of the electron transfer from $Ru(bpy)_3^{2+}$ in its triplet excited state depends on the wavelength energy as it seems to be the case for both materials. In other words, since CO_2 reduction occurs at the photocatalyst material, the overall efficiency would depend not only on excitation of $Ru(bpy)_3^{2+}$, that could be optimal for 450 nm, but also on the transfer of these electrons from Ru triplets to the inorganic material that we propose to depend on the wavelength energy.

To prove charge separation induced on the photocatalyst by light irradiation photocurrent measurements were carried out. A working electrode consisting of a thin film of the photocatalyst prepared by drop casting of an ethanol suspension of the materials under study deposited on top of a freshly clean FTO glass was irradiated with a Xe lamp, toggling on and off irradiation at regular time intervals. As can be seen in Fig. 6, changes in current intensity were recorded for NiL410 and CoM210 materials when irradiating with the full spectrum Xe lamp, and also exclusively in the visible region. It should be noted that the baseline current was not stable during the measurements, so only relative values for light-on and light-off onsets should be considered.

Electrochemical measurements using impedance spectroscopy with electrodes prepared for the best performing materials under study were carried out to determine the ohmic resistance of the charge transfer from the material to the electrolyte. The Nyquist plots of the corresponding measurements are given in Fig. S14 of the supporting information. In these measurements it was determined that Ni-based materials possess lower resistance to charge transfer to the electrolyte solution than their Co counterparts. It was also observed that charge migration to the electrolyte for LDH (both Ni and Co) increases upon calcination and formation of the corresponding mixed oxides. The easier charge migration for the case of NiL410 compared to CoL21 is in line with the formation of methane in the case of NiL410 that requires the transfer of 8 electrons as compared to CO formation observed for CoL21, which is a 2-electron process.

To provide some support to the role of Ni and Co materials as co-catalysts accepting electrons from $Ru(bpy)_3^{2+}$, transient absorption spectroscopy studies of the quenching of $Ru(bpy)_3^{2+}$ triplet excited state by LDH or MO were carried out monitoring at 360 nm. Upon irradiation of a solution of $Ru(bpy)_3^{2+}$ in acetonitrile the characteristic features corresponding to the intramolecular charge transfer triplet excited state of $Ru(bpy)_3^{2+}$ were recorded with a strong absorption at 370 nm, a less intense absorption band at 580 nm and the bleaching of the ground state appearing as negative signal at 440 nm (Figure S15). Addition of TEOA as electron donor quencher decreases the intensity of the signals, but without resulting in the appearance of any new signal in the UV-Vis range at 1 μs delay after the laser flash. If now NiL410 or CoM210 is added, an additional quenching is observed. This quenching by NiL410 or CoM210 is interpreted as supporting the occurrence of an electron transfer from $Ru(bpy)_3^{2+}$ triplet to NiL410 or CoM210. Furthermore, if instead of a N_2 atmosphere the cuvette is saturated with CO_2, stronger quenching of the $Ru(bpy)_3^{2+}$ triplet excited state is observed for both, in the presence of NiL410 and CoM210. These transient absorption measurements therefore provide direct evidence for the quenching of Ru $(bpy)_3^{2+}$ triplet state by the two most active materials in the present study, particularly in the presence of CO_2. Fig. 7 shows illustrative transient signals of the best performing photocatalysts.

3.3. Band energy diagram

The energies of the conduction and valence band of the various materials under study were experimentally determined by a combination of UPS data on the valence band maximum energy and the optical band gap of the materials measured by optical absorption spectroscopy. Details on the calculations to obtain the valence band energy values from the experimental UPS data are also provided in supporting information. Considering the presence of defects in the materials, interpolation of the onset of electron emission in the UPS measurements (Fig. 8) was used to determine the energy of the valence band maximum, whose energy was about 2 eV vs NHE. Optical band gap was calculated by plotting the Kubelka-Munk function, $(F(R)h\nu)^{1/n}$, vs the incident photon energy, and considering the materials as indirect band gap semiconductors (n = 2). Table 3 summarizes the band gap and band energy values for the most active samples in the present study. Several trends

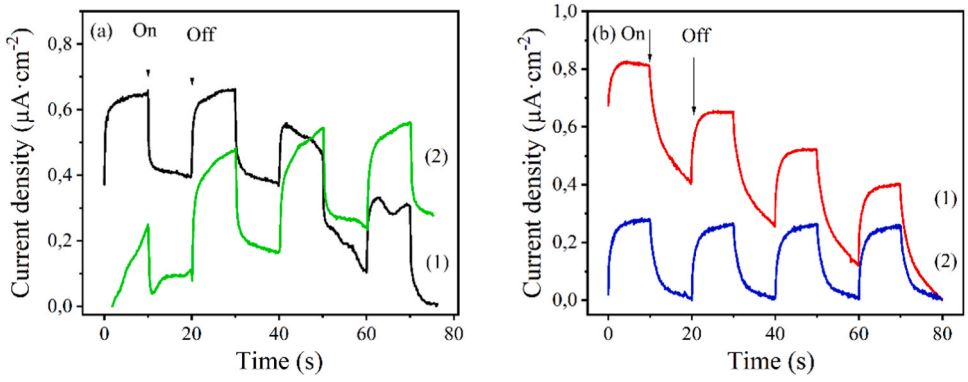

Fig. 6. Photocurrent measurements of NiL410 (a) and CoM210 (b) under irradiation with 300 W Xe lamp full spectrum (1) and in the visible region (2). Electrolyte: 0.1 M Na_2SO_4 in water. Electrochemical cell: LDH/FTO working electrode, Ag/AgCl reference electrode and Pt counter electrode. Light source: 300 W Xe lamp (with and without 380 cut-off filter, 100 mW/cm^2). Atmosphere: N_2.

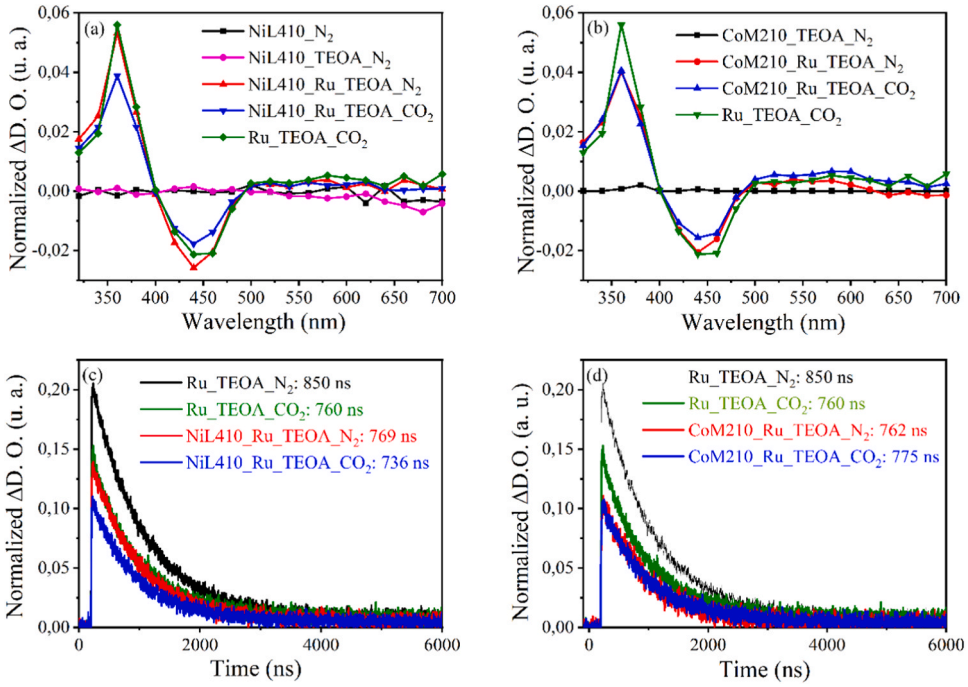

Fig. 7. Transient absorption spectra (a, b) upon excitation at 450 nm monitored at 0.5 μs and signal decay (c, d) monitored at 360 nm for NiL410 (a, c) and CoM210 (b, d).

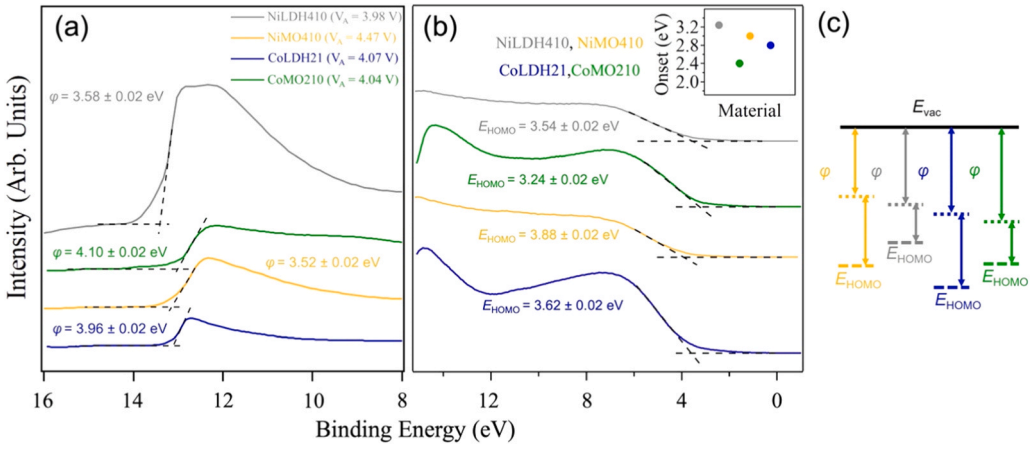

Fig. 8. (a) Work function (φ) and (b) energy of the HOMO (E_{HOMO}) of NiL410 (gray), NiM410 (yellow), CoL21 (blue), and CoM210 (green) extrapolated from the UPS measurements. The inset in (b) shows the onset energy of each material, with respect to the Fermi level (E_F). (c) Schematic illustrating the positions of the E_F with respect to the vacuum (E_{vac}), and positions of E_{HOMO} with respect to the E_F.

Table 3
Band energy parameters for some of the most active samples under study, obtained from Tauc plots and UPS spectra.

SAMPLE	E_g (eV)	VBM vs. NHE (eV)	CBM vs. NHE (eV)
NiL410	3.21	2.38	-0.83
NiM410	2.36	2.08	-0.28
CoL21	2.51	2.32	-0.19
CoM210	1.37	2.06	0.69

can be extracted from band energies, for instance, the valence band energy is higher for LDH materials compared to the mixed oxides with the same composition. Regarding conduction band potentials, they are lower (more negative) for Ni-containing samples compared to Co-based ones and lower for LDH compared to mixed oxides. Note that in the case of the black CoM210 sample, and due to its remarkably low bandgap, the conduction band potential has a positive value, while the Ni samples can reach a highly negative value.

As summary, Scheme 3 presents the experimental band energies for the most efficient samples also including the energy of the HOMO and LUMO states of $Ru(bpy)_3^{2+}$ and the oxidation potential of TEOA. According to this band diagram, upon excitation of $Ru(bpy)_3^{2+}$ and generation of the triplet excited states, TEOA could be the only species able to donate one electron to triplet excited state of $Ru(bpy)_3^{2+}$. On the other hand, the excited electron of $Ru(bpy)_3^{2+}$ can migrate to the conduction band of any of the solids under study. In the case of the Ni-based materials electron transfer from $Ru(bpy)_3^{2+}$ in its triplet excited state to the conduction band minimum will have enough energy to promote CO_2 reduction, both to form CO and CH_4. This mechanistic proposal based on thermodynamic potentials is in agreement with reported literature data for similar systems, in which $Ni(OH)_2$ has been used as cocatalyst for CO_2 reduction and photoinduced electron transfer from $Ru(bpy)_3^{2+}$

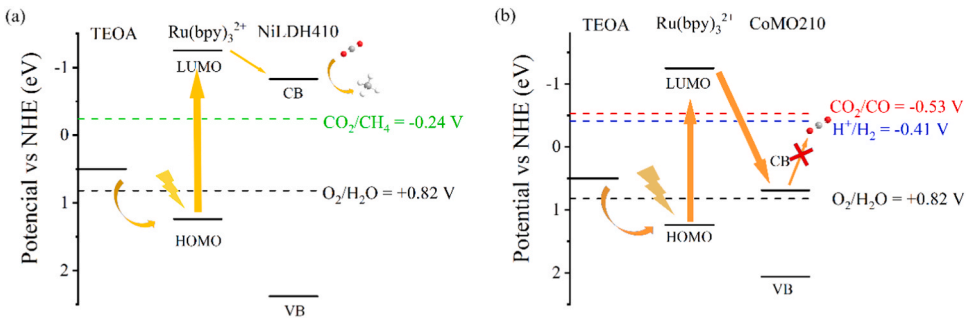

Scheme 3. Band energy diagram for NiL410 (a) and CoM210 (b).

triplet excited state to $Ni(OH)_2$ was similarly claimed [36].

On the contrary, due to the very narrow band gap of CoM210, the conduction band minimum of this material does not have negative enough potential to reduce CO_2 to CO. Therefore, according to the measurements, CoM210 should not be able to reduce CO_2. To find an explanation of the experimental evidence of photocatalytic CO evolution from CO_2 reduction using CoM210 as mediator, steady state photoluminescence measurements were carried out. The rationale is that although the conduction band minimum of CoM210 cannot reduce CO_2, there could be other upper states with higher reduction potential above the conduction band that could be responsible of this reduction. This could be possible on the case of CoM210 considering that its composition contains Ti and Al that could trap electrons in the material effectively, therefore, allowing the occurrence of reactions from upper electronic states. Experimental evidence for the existence of these states would be observation of defined emission bands at wavelengths shorter than the absorption edge of CoM210 around 800 nm. To confirm the existence of these upper states with higher reduction potential, a suit of photoluminescence spectra was recorded upon excitation of the solid at wavelengths in the range from 300 to 500 nm. It was observed that upon excitation at wavelengths shorter than 340 nm, an intense photoluminescence band at 340 nm was recorded, accompanied by a second, broader emission peak with a maximum intensity at 445 nm. A summary of these photoluminescence measurements is provided in Fig. 9.

Observation of a 340 nm emission from CoM210 can be interpreted as derived as electron-hole recombination with electrons in electronic states with higher energy than the conduction band minimum resulting in a photoemission at wavelengths shorter than the corresponding band gap. Similarly, the origin of the 445 nm emission peak is proposed to arise from photogenerated charge recombination for electronic states above the conduction band minimum. If this were the case, then these two electronic states responsible for the emission at 340 and 445 nm should have enough reduction potential to convert CO_2 into CO. An interesting point is that the first and most intense of these emissive states at λ_{em} 340 nm, that we propose to be involved on the photocatalytic reaction is totally absent in commercial Co_3O_4. In fact, in an analogous

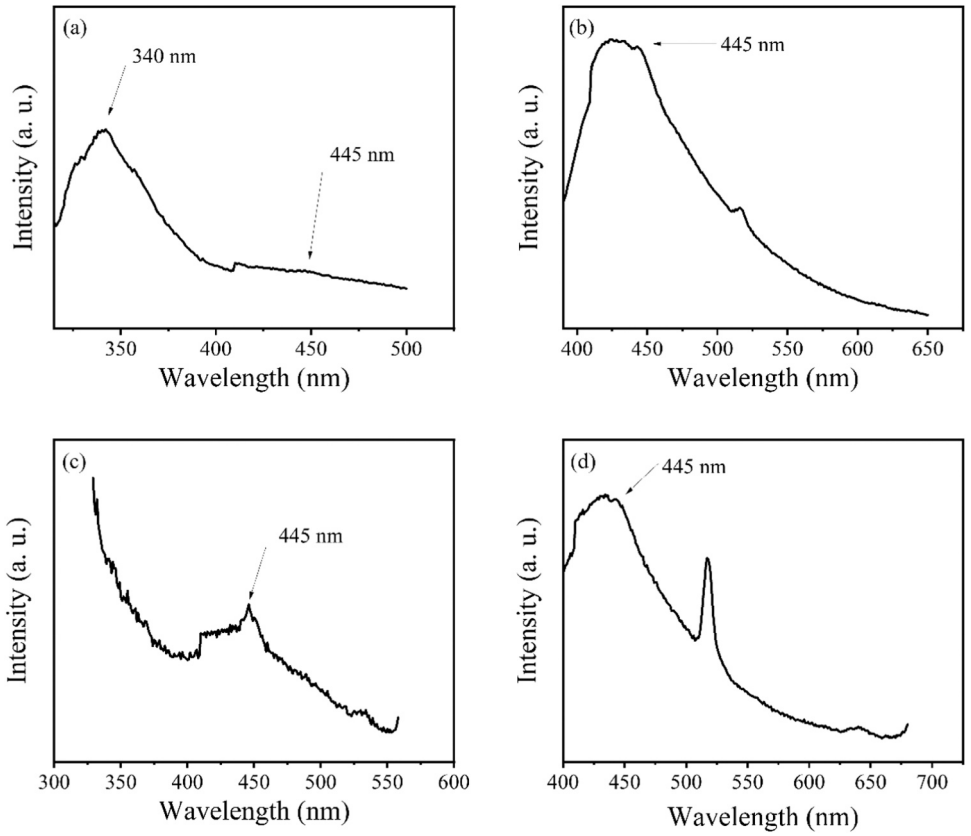

Fig. 9. Steady state fluorescence emission spectra of CoM210 upon excitation at 290 (a) and 360 nm (b) and comparison with commercial Co_3O_4 upon excitation at 290 (c) and 360 nm (d).

study on cobaltite only a weak emission peak at 445 nm could be observed. Therefore, it is proposed that the presence of Ti and Al metals in the composition of the trimetallic metal oxide is responsible for the implementation of some trapping states with higher energy in the conduction band that can participate in the photocatalytic generation of CO from CO_2. The present results illustrate the importance of doping and preparation of mixed oxides introducing other elements in the composition of an oxide semiconductor to improve or generate photocatalytic activity.

3.4. In-situ spectroscopic measurements

To try to explain the different product distribution for CO_2 photoreduction over NiL410 and CoM210, in-situ absorption measurements of CO_2 on NiL410 or CoM210 monitored by infrared spectroscopy were performed. The aim of the study was to detect different reaction intermediates that would indicate that CO_2 was being reducing following different mechanistic paths in these two materials. First, absorption of CO_2 in dark conditions was studied. In the case of CoM210, an increase in the intensity of the broad absorption bands centered at 1375 and 1512 cm^{-1} attributable to bi- and monodentate carbonates, respectively, was observed [56]. The band at 1636 cm^{-1} corresponds to an intrinsic absorption of the material, and its relative intensity decrease respect to the carbonate bands can be observed at longer CO_2 exposure times. Analogous studies on NiL410 could not be performed due to the strong intrinsic absorption of this material in this region. It should be noted that NiL410 exposed to the ambient for a long time should already contain carbonate species that originate a very strong absorption, making impossible to monitor minor changes in this region.

Upon irradiation of CoM210 exposed to moist CO_2 appearance of new weak absorptions assigned to $*HCO_3^-$ (1228 and 1427 cm^{-1}) and *COOH (1457 cm^{-1}) intermediates, in addition to the previously observed m-CO_3^{2-} (1540 cm^{-1}) and b-CO_3^{2-} (1373 cm^{-1}) bands was recorded [56,57]. Fig. 10 illustrates the main relevant IR regions of the in-situ study.

Two interesting features regarding the evolution of band intensity with exposure time to moist CO_2 and light irradiation should be commented. First, an increase in intensity of the bands assigned to $*HCO_3^-$ and *COOH (1457 cm^{-1}) reaction intermediates between the beginning of the experiment and 30 min irradiation can be observed. These species have been reported in the literature to be reaction intermediates for the CO_2 reduction to CO [56,58,59]. However, these bands disappear after 60 min of irradiation. A possible explanation for this disappearance at longer irradiation times could be that photocatalytic CO_2 reduction has an initial induction period, where reaction rate is not very high, and the intermediates have enough lifetime to accumulate, being easily observed. Once this induction period is overcome, reaction rate increases, and the conditions do not allow the accumulation of reaction intermediates over the surface of the photocatalyst.

The other distinct feature is that, when the study is performed under visible light irradiation, relative intensity of the intrinsic material band at 1636 cm^{-1} respect to the carbonate bands is more or less constant. A possible explanation for this behavior, is that CO_2 molecules are being consumed in the photocatalytic process and transformed to CO, so they cannot accumulate in the form of carbonate over the surface of the material as much as in dark conditions.

Considering the detection of *COOH, a plausible mechanism of CO formation according to the literature is proposed in Scheme 4.

4. Conclusions

In the present study a series of trimetallic LDH materials containing

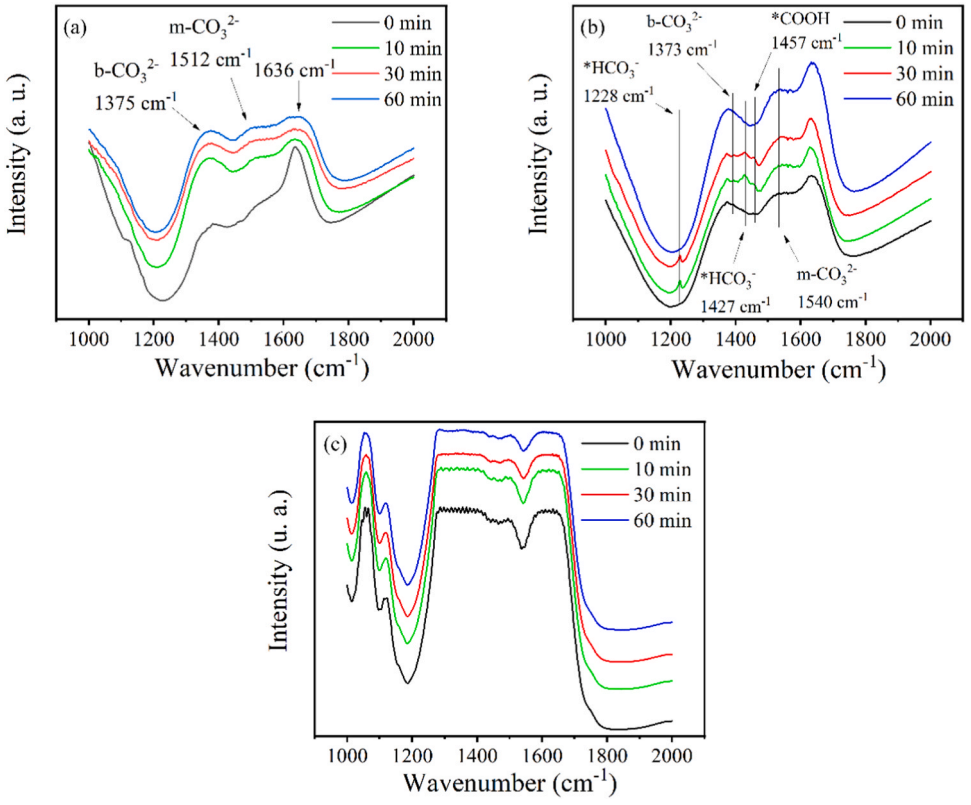

Fig. 10. In-situ infrared absorption spectra recorded in the region 2000–1000 cm^{-1} for CoM210 in dark (a) and under visible light irradiation (b). In-situ infrared absorption spectrum for NiL410 in the same region (c). It should be noted that the plateau between 1300 and 1700 cm^{-1}, due to saturation of the detector because the strong intrinsic absorption of the material in this region, does not allow a proper analysis of CO_2 reduction intermediates. Measurement conditions: water saturated CO_2 flow (30 ml/min), T: 50 ºC. Light source: 300 W Xe lamp equipped with a 380 nm cut-off filter.

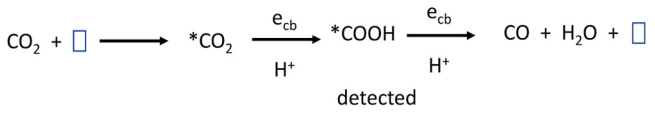

Scheme 4. Proposed reaction mechanism, in which □ means an adsorption/catalytic site, * means that the species is adsorbed on the surface and e_{cb} corresponds to a conduction band electron.

Ti in their chemical composition have been successfully synthesized showing the flexibility that the synthesis of LDHs offers to prepare multimetallic photocatalysts. Utilization of $Ti^{(IV)}$ bis(ammonium-lactate)dihydroxide complex as Ti source and methanol as solvent for the synthesis drives the particle growth into a morphology composed of spherical aggregates of LDH nanosheets. Modulating several synthesis parameters, such as chemical composition, cation ratio or precursor concentration, allows to study the influence of these parameters on the photocatalytic activity for CO_2 reduction.

Of all characterized materials, NiL410 and CoM210 stand out as the best performing photocatalysts for CO_2 photoreduction. In the case of NiL410, CH_4 was evolved from CO_2, with a production rate of 4.59 μmol/h and a selectivity above 86%, which ranks it as the best performing material in the literature for CH_4 production from CO_2 when H_2O is employed as the proton source. On the other hand, CoM210 generates similar amounts of CO and H_2, with a production comparable to the state of the art.

The analysis of the materials by spectroscopic characterization techniques (UV-Vis DRS, UPS, TAS, fluorescence and in situ FTIR) gave the necessary data to construct the band energy diagram to explain the selectivity of the generated products and the relationship with the chemical composition of the materials, and the photocatalytic activity. Experimental evidence of the proposed mechanism, in which the Ru $(bpy)_3^{2+}$ complex acts as the light harvester and then transfers the photogenerated electrons to the LDH or mixed oxide material, which in turn reduces the CO_2 molecule, are provided. One important finding was the operation in the photocatalytic activity of upper electronic states in mixed oxides with stronger reduction potential due to the combination of metals. Further evidence of the presence of these upper states would require ultrafast transient absorption studies to detect them and follow their reactivity.

This study constitutes an example of design of materials with specific properties that allow to modulate the selectivity to different products in CO_2 photocatalytic reduction. Further research on this field could improve the performance of these materials, for example by including additional cations in the structure or tuning the composition and structure to achieve high selectivity to other valuable products, such as alcohols or C_{2+} hydrocarbons.

CRediT authorship contribution statement

Juan Francisco Sánchez-Royo: Data curation. **Josep Albero:** Investigation, Data curation. **Archit Dhingra:** Data curation. **Mahesh Eledath-Changarath:** Investigation. **Manuel Molina-Muriel:** Writing – original draft, Investigation, Data curation. **Hermenegildo García:** Writing – review & editing, Supervision. **Antonio Ribera:** Writing – review & editing, Supervision.

Declaration of Competing Interest

The authors declare that they have no known competing financial interests or personal relationships that could have appeared to influence the work reported in this paper.

Data Availability

Data will be made available on request.

Acknowledgments

Financial support by the Spanish Ministry of Science and Innovation (CEX-2021–001230-S, PID2021–0126071-OB-CO21 and PID2021–125907NB-I00 funded by MCIN/AEI/10.13039/501100011033/ FEDER) and Generalitat Valenciana (Prometeo 2021–038, CIPROM-2022–60 and Advanced Materials Program MFA-2022–023 and MFA-2022–057 with funding from European Union Next Generation EU PRTR-C17.I1) are gratefully acknowledged. M. M. thanks the Universitat Politècnica de Valencia for a postgraduate scholarship.

Appendix A. Supporting information

Supplementary data associated with this article can be found in the online version at doi:10.1016/j.jcou.2024.102810.

References

[1] C. Lv, X. Bai, S. Ning, C. Song, Q. Guan, B. Liu, Y. Li, J. Ye, Nanostructured materials for photothermal carbon dioxide hydrogenation: regulating solar utilization and catalytic performance, ACS Nano 17 (2023) 1725–1738, https://doi.org/10.1021/acsnano.2c09025.
[2] A. Rehman, G. Nazir, K.Y. Rhee, S. Park, Electrocatalytic and photocatalytic sustainable conversion of carbon dioxide to value-added chemicals: State-of-the-art progress, challenges, and future directions, J. Environ. Chem. Eng. 10 (2022) 108219, https://doi.org/10.1016/j.jece.2022.108219.
[3] S. Shin, H. Choi, S. Ringe, D.H. Won, H. Oh, D.H. Kim, T. Lee, D. Nam, H. Kim, C. H. Choi, A unifying mechanism for cation effect modulating C1 and C2 productions from CO2 electroreduction, Nat. Commun. 13 (2022) 5482, https://doi.org/10.1038/s41467-022-33199-8.
[4] S. Cheng, Z. Sun, K.H. Lim, T.Z.H. Gani, T. Zhang, Y. Wang, H. Yin, K. Liu, H. Guo, T. Du, L. Liu, G.K. Li, Z. Yin, S. Kawi, Emerging strategies for CO2 photoreduction to CH4: from experimental to data-driven design, Adv. Energy Mater. 12 (2022) 2200389, https://doi.org/10.1002/aenm.202200389.
[5] D. Wu, F. Jiao, Q. Lu, Progress and Understanding of CO2/CO electroreduction in flow electrolyzers, ACS Catal. 12 (2022) 12993–13020, https://doi.org/10.1021/acscatal.2c03348.
[6] J. Albero, Y. Peng, H. García, Photocatalytic CO2 Reduction to C2+ Products, ACS Catal. 10 (2020) 5734–5749, https://doi.org/10.1021/acscatal.0c00478.
[7] X. Jiao, K. Zheng, L. Liang, X. Li, Y. Sun, Y. Xie, Fundamentals and challenges of ultrathin 2D photocatalysts in boosting CO2 photoreduction, Chem. Soc. Rev. 49 (2020) 6592–6604, https://doi.org/10.1039/D0CS00332H.
[8] Z. Li, R. Shi, Y. Ma, J. Zhao, T. Zhang, Photodriven CO2 hydrogenation into diverse products: recent progress and perspective, J. Phys. Chem. Lett. 13 (2022) 5291–5303, https://doi.org/10.1021/acs.jpclett.2c01159.
[9] S. Yao, B. Sun, P. Zhang, Z. Tian, H. Yin, Z. Zhang, Anchoring ultrafine Cu2O nanocluster on PCN for CO2 photoreduction in water vapor with much improved stability, Appl. Catal. B: Environ. 317 (2022) 121702, https://doi.org/10.1016/j.apcatb.2022.121702.
[10] X. Li, J. Yu, M. Jaroniec, X. Chen, Cocatalysts for selective photoreduction of CO2 into solar fuels, Chem. Rev. 119 (2019) 3962–4179, https://doi.org/10.1021/acs.chemrev.8b00400.
[11] D. Li, M. Kassymova, X. Cai, S. Zang, H. Jiang, Photocatalytic CO2 reduction over metal-organic framework-based materials, Coord. Chem. Rev. 412 (2020) 213262, https://doi.org/10.1016/j.ccr.2020.213262.
[12] W. Zhan, H. Gao, Y. Yang, X. Li, Q. Zhu, Rational design of metal–organic framework-based materials for photocatalytic CO2 reduction, Adv. Energy Sustain. Res. 3 (2022) 2200004, https://doi.org/10.1002/aesr.202200004.
[13] F. Lv, W. Zhang, L. He, X. Bai, Y. Song, Y. Zhao, 3D porous flower-like CoAl2O4 to boost the photocatalytic CO2 reduction reaction, J. Mater. Chem. A 11 (2023) 2826–2835, https://doi.org/10.1039/D2TA08947E.
[14] L. Li, X. Dai, D. Chen, Y. Zeng, Y. Hu, X.W. Lou, Steering catalytic activity and selectivity of CO2 photoreduction to syngas with hydroxy-rich Cu2S@ROH-NiCo2O3 double-shelled nanoboxes, Angew. Chem. Int. Ed. 61 (2022) e202205839, https://doi.org/10.1002/anie.202205839.
[15] Y. Zhao, M. Que, J. Chen, C. Yang, MXenes as co-catalysts for the solar-driven photocatalytic reduction of CO2, J. Mater. Chem. C. 8 (2020) 16258–16281, https://doi.org/10.1039/D0TC02979C.
[16] J. Low, B. Cheng, J. Yu, M. Jaroniec, Carbon-based two-dimensional layered materials for photocatalytic CO2 reduction to solar fuels, Energy Storage Mater. 3 (2016) 24–35, https://doi.org/10.1016/j.ensm.2015.12.003.
[17] S. Cheng, Z. Sun, K.H. Lim, A.A. Wibowo, T. Zhang, T. Du, L. Liu, H.T. Nguyen, G. K. Li, Z. Yin, S. Kawi, Dual-Defective Two-Dimensional/Two-Dimensional Z-Scheme Heterojunctions for CO2 Reduction, ACS Catal. 13 (2023) 7221–7229, https://doi.org/10.1021/acscatal.3c00219.
[18] P. Miao, J. Zhao, R. Shi, Z. Li, Y. Zhao, C. Zhou, T. Zhang, Layered double hydroxide engineering for the photocatalytic conversion of inactive carbon and nitrogen molecules, ACS EST Eng. 2 (2022) 1088–1102, https://doi.org/10.1021/acsestengg.1c00489.

[19] X. Bian, S. Zhang, Y. Zhao, R. Shi, T. Zhang, Layered double hydroxide-based photocatalytic materials toward renewable solar fuels production, InfoMat 3 (2021) 719–738, https://doi.org/10.1002/inf2.12192.
[20] L. Tan, Z. Wang, Y. Zhao, Y. Song, Recent Progress on Nanostructured Layered Double Hydroxides for Visible-Light-Induced Photoreduction of CO2, Chem. Asian J 15 (2020) 3380–3389, https://doi.org/10.1002/asia.202000963.
[21] X. Zhang, S. Li, Mechanochemical approach for synthesis of layered double hydroxides, Appl. Surf. Sci. 274 (2013) 158–163, https://doi.org/10.1016/j.apsusc.2013.03.003.
[22] S. Bai, T. Li, H. Wang, L. Tan, Y. Zhao, Y. Song, Scale-up synthesis of monolayer layered double hydroxide nanosheets via separate nucleation and aging steps method for efficient CO2 photoreduction, Chem. Eng. J. 419 (2021) 129390, https://doi.org/10.1016/j.cej.2021.129390.
[23] F. Cavani, F. Trifirò, A. Vaccari, Hydrotalcite-type anionic clays: Preparation, properties and applications, Catal. Today 11 (1991) 173–301, https://doi.org/10.1016/0920-5861(91)80068-K.
[24] X. Xiong, Y. Zhao, R. Shi, W. Yin, Y. Zhao, G.I.N. Waterhouse, T. Zhang, Selective photocatalytic CO2 reduction over Zn-based layered double hydroxides containing tri or tetravalent metals, Sci. Bull. 65 (2020) 987–994, https://doi.org/10.1016/j.scib.2020.03.032.
[25] R. Wang, X. Wang, Y. Xiong, Y. Hou, Y. Wang, J. Ding, Q. Zhong, Modulation of Trivalent/Tetravalent Metallic Elements in Ni-Based Layered Double Hydroxides for Photocatalytic CO2 Reduction, ACS Appl. Mater. Interfaces 14 (2022) 35654–35662, https://doi.org/10.1021/acsami.2c07940.
[26] M. Li, Z. Zuo, S. Zhang, High-Density Ultrafine Au Nanocluster-Doped Co-LDH Nanocages for Enhanced Visible-Light-Driven CO2 Reduction, ACS Catal. 13 (2023) 11815–11824, https://doi.org/10.1021/acscatal.3c02486.
[27] S. Yu, L. Tan, S. Bai, C. Ning, G. Liu, H. Wang, B. Liu, Y. Zhao, Y. Song, Rational regulation of electronic structure in layered double hydroxide via vanadium incorporation to trigger highly selective CO2 photoreduction to CH4, Small 18 (2022) 2202334, https://doi.org/10.1002/smll.202202334.
[28] F. Wang, R. Fang, X. Zhao, X. Kong, T. Hou, K. Shen, Y. Li, Ultrathin Nanosheet Assembled Multishelled Superstructures for Photocatalytic CO2 Reduction, ACS Nano 16 (2022) 4517–4527, https://doi.org/10.1021/acsnano.1c10958.
[29] Y. Su, Z. Song, W. Zhu, Q. Mu, X. Yuan, Y. Lian, H. Cheng, Z. Deng, M. Chen, W. Yin, Y. Peng, Visible-light photocatalytic CO2 reduction using metal-organic framework derived Ni(OH)2 nanocages: a synergy from multiple light reflection, static charge transfer, and oxygen vacancies, ACS Catal. 11 (2021) 345–354, https://doi.org/10.1021/acscatal.0c04020.
[30] Z. Wang, S. Xu, L. Tan, G. Liu, T. Shen, C. Yu, H. Wang, Y. Tao, X. Cao, Y. Zhao, Y. Song, 600 nm-driven photoreduction of CO2 through the topological transformation of layered double hydroxides nanosheets, Appl. Catal. B: Environ. 270 (2020) 118884, https://doi.org/10.1016/j.apcatb.2020.118884.
[31] Z. Li, R. Shi, J. Zhao, T. Zhang, Ni-based catalysts derived from layered-double-hydroxide nanosheets for efficient photothermal CO2 reduction under flow-type system, Nano Res. 14 (2021) 4828–4832, https://doi.org/10.1007/s12274-021-3436-6.
[32] C. Li, R. Guo, Z. Zhang, T. Wu, Y. Liu, Z. Zhou, M. Aisanjiang, W. Pan, Constructing CoAl-LDO/MoO3−x S-scheme heterojunctions for enhanced photocatalytic CO2 reduction, J. Colloid Interface Sci. 650 (2023) 983–993, https://doi.org/10.1016/j.jcis.2023.07.068.
[33] F. Chen, L. Zhou, C. Peng, D. Zhang, L. Li, D. Xue, Y. Yu, Bimetal-organic layer-derived ultrathin lateral heterojunction with continuous semi-coherent interfaces for boosting photocatalytic CO2 reduction, Appl. Catal. B: Environ. 331 (2023) 122689, https://doi.org/10.1016/j.apcatb.2023.122689.
[34] G. Qian, W. Lyu, X. Zhao, J. Zhou, R. Fang, F. Wang, Y. Li, Efficient photoreduction of diluted CO2 to tunable syngas by Ni−Co dual sites through d-band center manipulation, Angew. Chem. Int. Ed. 61 (2022) e202210576, https://doi.org/10.1002/anie.202210576.
[35] L. Tan, S. Xu, Z. Wang, X. Hao, T. Li, H. Yan, W. Zhang, Y. Zhao, Y. Song, 600 nm induced nearly 99% selectivity of CH4 from CO2 photoreduction using defect-rich monolayer structures, Cell Rep. Phys. Sci. 2 (2021) 100322, https://doi.org/10.1016/j.xcrp.2021.100322.
[36] K. Lu, Y. Li, F. Zhang, M. Qi, X. Chen, Z. Tang, Y.M.A. Yamada, M. Anpo, M. Conte, Y. Xu, Rationally designed transition metal hydroxide nanosheet arrays on graphene for artificial CO2 reduction, Nat. Commun. 11 (2020) 5181, https://doi.org/10.1038/s41467-020-18944-1.
[37] S. Bai, Z. Wang, L. Tan, G.I.N. Waterhouse, Y. Zhao, Y. Song, 600 nm Irradiation-Induced Efficient Photocatalytic CO2 Reduction by Ultrathin Layered Double Hydroxide Nanosheets, Ind. Eng. Chem. Res 59 (2020) 5848–5857, https://doi.org/10.1021/acs.iecr.0c00522.
[38] L. Tan, S. Xu, Z. Wang, Y. Xu, X. Wang, X. Hao, S. Bai, C. Ning, Y. Wang, W. Zhang, Y.K. Jo, S. Hwang, X. Cao, X. Zheng, H. Yan, Y. Zhao, H. Duan, Y. Song, Highly selective photoreduction of co2 with suppressing H2 evolution over monolayer layered double hydroxide under irradiation above 600nm, Angew. Chem. Int. Ed. 58 (2019) 11860–11867, https://doi.org/10.1002/anie.201904246.
[39] A. Fasolini, N. Sangiorgi, E. Tosi Brandi, A. Sangiorgi, F. Mariani, E. Scavetta, A. Sanson, F. Basile, Increased efficiency and stability of Dye-Sensitized Solar Cells (DSSC) photoanode by intercalation of Eosin Y into Zn/Al layered double hydroxide, Appl. Clay. Sci. 212 (2021) 106219, https://doi.org/10.1016/j.clay.2021.106219.
[40] H. Pang, F. Ichihara, X. Meng, L. Li, Y. Xiao, W. Zhou, J. Ye, Selectivity control of photocatalytic CO2 reduction over ZnS-based nanocrystals: A comparison study on the role of ionic cocatalysts, J. Energy Chem. 86 (2023) 391–398, https://doi.org/10.1016/j.jechem.2023.07.031.
[41] Y. Sun, L. Li, X. Li, Y. Feng, F. Chen, L. Li, Y. Yu, Regulating activity and selectivity of photocatalytic CO2 reduction on cobalt by rare earth compounds, ACS Appl. Mater. Interfaces 15 (2023) 16621–16630, https://doi.org/10.1021/acsami.2c20402.
[42] M. Molina-Muriel, Y. Peng, H. García, A. Ribera, Increased photocatalytic activity and selectivity towards methane of trimetallic NiTiAl-LDH, J. Alloy. Compd. 897 (2022) 163124, https://doi.org/10.1016/j.jallcom.2021.163124.
[43] Z. Lu, L. Qian, W. Xu, Y. Tian, M. Jiang, Y. Li, X. Sun, X. Duan, Dehydrated layered double hydroxides: Alcohothermal synthesis and oxygen evolution activity, Nano Res. 9 (2016) 3152–3161, https://doi.org/10.1007/s12274-016-1197-4.
[44] Y. Zhao, B. Li, Q. Wang, W. Gao, C.J. Wang, M. Wei, D.G. Evans, X. Duan, D. O'Hare, NiTi-Layered double hydroxides nanosheets as efficient photocatalysts for oxygen evolution from water using visible light, Chem. Sci. 5 (2014) 951–958, https://doi.org/10.1039/C3SC52546E.
[45] S. Tonda, S. Kumar, M. Bhardwaj, P. Yadav, S. Ogale, g-C3N4/NiAl-LDH 2D/2D Hybrid Heterojunction for High-Performance Photocatalytic Reduction of CO2 into Renewable Fuels, ACS Appl. Mater. Interfaces 10 (2018) 2667–2678, https://doi.org/10.1021/acsami.7b18835.
[46] K. Wang, L. Zhang, Y. Su, D. Shao, S. Zeng, W. Wang, Photoreduction of carbon dioxide of atmospheric concentration to methane with water over CoAl-layered double hydroxide nanosheets, J. Mater. Chem. A 6 (2018) 8366–8373, https://doi.org/10.1039/C8TA01309H.
[47] A. Ziarati, A. Badiei, R. Grillo, T. Burgi, 3D Yolk@Shell TiO2–x/LDH architecture: tailored structure for visible light CO2 conversion, ACS Appl. Mater. Interfaces 11 (2019) 5903–5910, https://doi.org/10.1021/acsami.8b17232.
[48] Y. Zhao, L. Zheng, R. Shi, S. Zhang, X. Bian, F. Wu, X. Cao, G.I.N. Waterhouse, T. Zhang, Alkali etching of layered double hydroxide nanosheets for enhanced photocatalytic N2 reduction to NH3, Adv. Energy Mater. 10 (2020) 2002199, https://doi.org/10.1002/aenm.202002199.
[49] X. Zhang, Y. Zhao, Y. Zhao, R. Shi, G.I.N. Waterhouse, T. Zhang, A simple synthetic strategy toward defect-rich porous monolayer NiFe-layered double hydroxide nanosheets for efficient electrocatalytic water oxidation, Adv. Energy Mater. 9 (2019) 1900881, https://doi.org/10.1002/aenm.201900881.
[50] A. Primo, A. Rendón-Patiño, C. Bucur, A. Jurca, B. Cojocaru, V.I. Parvulescu, H. Garcia, Doped microporous graphitic carbons as metal-free catalysts for the selective hydrogenation of alkynes to alkenes, J. Catal. 405 (2022) 355–362, https://doi.org/10.1016/j.jcat.2021.11.034.
[51] W. Chen, B. Han, C. Tian, X. Liu, S. Liang, H. Deng, Z. Lin, MOFs-derived ultrathin holey Co3O4 nanosheets for enhanced visible light CO2 reduction, Appl. Catal. B: Environ. 244 (2019) 996–1003, https://doi.org/10.1016/j.apcatb.2018.12.045.
[52] M.C. Biesinger, B.P. Payne, A.P. Grosvenor, L.W.M. Lau, A.R. Gerson, R.S.C. Smart, Resolving surface chemical states in XPS analysis of first row transition metals, oxides and hydroxides: Cr, Mn, Fe, Co and Ni, Appl. Surf. Sci. 257 (2011) 2717–2730, https://doi.org/10.1016/j.apsusc.2010.10.051.
[53] M.C. Biesinger, L.W.M. Lau, A.R. Gerson, R.S.C. Smart, Resolving surface chemical states in XPS analysis of first row transition metals, oxides and hydroxides: Sc, Ti, V, Cu and Zn, Appl. Surf. Sci. 257 (2010) 887–898, https://doi.org/10.1016/j.apsusc.2010.07.086.
[54] M.C. Biesinger, B.P. Payne, L.W.M. Lau, A. Gerson, R.S.C. Smart, X-ray photoelectron spectroscopic chemical state quantification of mixed nickel metal, oxide and hydroxide systems, Surf. Interface Anal. 41 (2009) 324–332, https://doi.org/10.1002/sia.3026.
[55] X. Hao, L. Tan, Y. Xu, Z. Wang, X. Wang, S. Bai, C. Ning, J. Zhao, Y. Zhao, Y. Song, Engineering active Ni sites in ternary layered double hydroxide nanosheets for a highly selective photoreduction of CO2 to CH4 under irradiation above 500 nm, Ind. Eng. Chem. Res 59 (2020) 3008–3015, https://doi.org/10.1021/acs.iecr.9b06464.
[56] L. Liu, C. Zhao, J.T. Miller, Y. Li, Mechanistic study of CO2 photoreduction with H2O on Cu/TiO2 nanocomposites by in Situ X-ray absorption and infrared spectroscopies, J. Phys. Chem. C. 121 (2017) 490–499, https://doi.org/10.1021/acs.jpcc.6b10835.
[57] R. Wang, Z. Wang, X. Shang, Y. Yang, J. Ding, Q. Zhong, A novel S-scheme heterojunction constructed by Ti-based hydrotalcite decorating MOFs for boosting CO2-to-CO photoreduction and mechanism insights, J. Mater. Chem. A 11 (2023) 630–641, https://doi.org/10.1039/D2TA08349C.
[58] R. Wang, Z. Wang, S. Wan, Q. Liu, J. Ding, Q. Zhong, Facile layer regulation strategy of layered double hydroxide nanosheets for artificial photosynthesis and mechanism insight, Chem. Eng. J. 434 (2022) 134434, https://doi.org/10.1016/j.cej.2021.134434.
[59] R. Wang, Z. Wang, Z. Qiu, S. Wan, J. Ding, Q. Zhong, Nanoscale 2D g-C3N4 decorating 3D hierarchical architecture LDH for artificial photosynthesis and mechanism insight, Chem. Eng. J. 448 (2022) 137338, https://doi.org/10.1016/j.cej.2022.137338.